Low Temperature Physics/Fizika Nizkikh Temperatur, 2014, v. 40, No. 7, pp. 825–834

# Electronic structure and x-ray magnetic circular dichroism in the $Mn_3CuN$ perovskite

V.N. Antonov and L.V. Bekenov

*Institute for Metal Physics, 36 Vernadsky Str., Kiev 03142, Ukraine*
E-mail: antonov@imp.kiev.ua

Received February 20, 2014, published online May 21, 2014

The electronic and magnetic structures of $Mn_3CuN$ are investigated theoretically from first principles using the fully relativistic Dirac LMTO band structure method. $Mn_3CuN$ possesses a magnetic phase transition at $T_C$ = 143 K from a high temperature paramagnetic phase to a low temperature ferromagnetic one with a noncollinear magnetic structure. The transition is accompanied by a structural change from the cubic to the tetragonal lattice. In low temperature phase two Cu moments and two Mn moments ($Mn_2$ and $Mn_3$) ferromagnetically align along the *c* axis while other four $Mn_1$ magnetic moments are canted from the *c* axis to [111] direction by angle $\Theta = \pm 76.2$. The x-ray absorption spectra and x-ray magnetic circular dichroism (XMCD) spectra of $Mn_3CuN$ are investigated theoretically from first principles. The origin of the XMCD spectra in the $Mn_3CuN$ compound is examined. The calculated results are compared with the experimental data.

PACS: 75.50.Cc Other ferromagnetic metals and alloys;
71.20.Lp Intermetallic compounds;
71.15.Rf Relativistic effects.

Keywords: electronic structure, ternary manganese compounds.

## 1. Introduction

Ternary manganese compounds with a formula $Mn_3MX$ (M = Ga, Sn, Zn, Cu and X = C and N) and the cubic crystal structure of a perovskite type have attracted much interest due to the peculiar relationship between lattice and magnetism which leads to a large variety of magnetic orderings and structural transformations [1–9]. The control of magnetostructural correlations in a magnetic metal is extremely important in various advanced industrial applications. By tuning the magnetostructural correlations, various useful functions, such as ferromagnetic shape memory effect [10,11], negative thermal expansion [12], and magnetocaloric effects [13,14], have been developed. In particular, magnetostruction [15], one of the most important properties of a magnetic metal, has a high potential for practical applications, such as in actuators and magnetic switching devices.

One of the most attractive materials exhibiting magnetostructural correlations are antiperovskite manganese nitrides $Mn_3MN$ (M: transitional metal or semiconducting element) [8]. The antiperovskites possess so called magnetovolume effect (MVE), such as negative thermal expansion (NTE) [16–20]. A large volume expansion in antiperovskite manganese nitrides is triggered by magnetic transition from high-temperature (high-T) paramagnetic (PM) phase to low-temperature (low-T) antiferromagnetic (AF) or ferromagnetic (FM) ordered phases. Another type of the peculiar relationship between the lattice and magnetism is the shape deformation by external magnetic field or magnetostriction. Magnetostriction often occurs without the volume change and it provides information complementary to that obtained from the volume effect. From a technological viewpoint, shape control by external field is one of the most important functions of metallic ferromagnets and has high potential in the design of actuating devices and sensors [15]. Shibayama and Takenaka [21] explored the magnetostriction in $Mn_3CuN$. It is exceptionally ferromagnetic among antiperovskite manganese nitrides $Mn_3MN$ (M: Zn, Ga, Ag, etc.) most of which are antiferromagnetic. They found that $Mn_3CuN$ exhibits large magnetostriction up to 0.2% even in a polycrystalline. This magnetostriction can be reasonably explained in terms of the rearrangement of thermoelastic martensite variants by the magnetic field; that is, $Mn_3CuN$ can be classified as a FM shape memory alloy. Generally, magnetostriction originates from anisotropy in the wave function of the electrons that induce a magnetic moment. The anisotropy of the electron cloud produces magnetocrystalline anisotropy,

© V.N. Antonov and L.V. Bekenov 2014

that is, a tendency for a magnetic moment to align along a certain crystallographic direction, which is a dominant factor for magnetostriction in an FM shape memory alloy. In the case of $Mn_3CuN$, however, large magnetocrystalline anisotropy is not expected because the 3*d* orbitals of Mn are almost half-filled, resulting in an almost isotropic electron cloud, and because the crystallographic anisotropy of $Mn_3CuN$ is much smaller than that of typical FM shape memory alloys.

$Mn_3CuN$ undergoes the first-order transition from a high-T PM to a low-T FM phase at the Curie temperature $T_C$ = 143 K [22]. At $T_C$, the structural deformation simultaneously occurs from a high-T cubic unit cell ($Pm3m$) to a low-T tetragonal one with shorter $c$ axis, $T_1^-$ ($c/a < 1$, $P4/mmm$), but the volume is conservative. The lattice parameters $a$ and $c$ are 3.9075 Å and 3.8502 Å at 100 K, respectively, and the tetragonality $c/a$ is estimated to be 0.9853 [23]. In $Mn_3CuN$ the results of neutron diffraction show that the magnetic moments of Mn atoms are much smaller than the 4–5 $\mu_B$ observed in other ordered manganese alloys [8]. This result indicates a strong itinerant character of 3*d* electrons of Mn atoms in $Mn_3CuN$.

The energy band structure of the $Mn_3MX$ (M=Ga, Sn, Zn, Cu and X=C and N) systems has been calculated by various methods [24–28]. In the present study, we focus our attention on the theoretical investigation of the x-ray magnetic circular dichroism (XMCD) in the low temperature non-collinear phase of $Mn_3CuN$. Takenaka *et al*. [29] explored the magnetic states of Mn and Cu in $Mn_3CuN$ using the x-ray magnetic circular dichroism. They evaluated the spin and orbital magnetic moments, $m_s$ and $m_l$, respectively, not only for Mn but also for Cu. The theoretical investigations of the origin of the XMCD spectra at the *K* edges of Mn in the ferromagnetic cubic phases of $Mn_3GaC$ and $Mn_3ZnC$ were carried out in Ref. 27 using the LSDA approximation. The electronic and magnetic structure as well as the XMCD spectra in the low temperature noncollinear $Mn_3ZnC$ perovskite were studied in Ref 30.

This paper is organized as follows. Section 2 presents a description of the perovskite $Mn_3CuN$ crystal and magnetic structures as well as the computational details. Section 3 is devoted to the electronic structure and XMCD spectra of the $Mn_3CuN$ compound calculated in the fully relativistic Dirac LMTO band structure method. The calculated results are compared with the available experimental data. Finally, the results are summarized in Sec. 4.

## 2. Crystal structure and computational details

*General properties of spin density waves*. The magnetic configuration of an incommensurate spin spiral shows the magnetic moments of certain atomic planes varying in direction. The variation has a well-defined period determined by a wave vector **q**. When the magnetic moment is confined to the lattice sites the magnetization **M** varies as [31]

$$\mathbf{M}(\mathbf{r}_n) = m_n \begin{bmatrix} \cos(\mathbf{q}\mathbf{r}_n + \varphi_n)\sin(\theta_n) \\ \sin(\mathbf{q}\mathbf{r}_n + \varphi_n)\sin(\theta_n) \\ \cos(\theta_n) \end{bmatrix}, \quad (1)$$

where the polar coordinates are used and $m_n$ is the magnetic moment of atom $n$ with a phase $\varphi_n$ at the position $\mathbf{r}_n$. Here we consider only planar spirals, that is, $\theta_n = \pi/2$ which also give the minimum of the total energy. The magnetization of Eq. (1) is not translationally invariant but transforms as

$$\mathbf{M}(\mathbf{r}+\mathbf{R}) = D(\mathbf{qr})\mathbf{M}(\mathbf{r}), \quad (2)$$

where **R** is a lattice translation and $D$ is a rotation around the $z$ axis. A spin spiral with a magnetization in a general point **r** in space can be defined as a magnetic configuration which transforms according to Eq. (2). Since the spin spiral describes a spatially rotating magnetization, it can be correlated with a frozen magnon.

Because the spin spiral breaks translational symmetry, the Bloch theorem is no longer valid. Computationally, one should use large super-cells to obtain total-energy of the spin spirals. However, when the spin-orbit interaction is neglected spins are decoupled from the lattice and only the relative orientation of the magnetic moments is important. Then, one can define generalized translations which contain translations in the real space and rotations in the spin space [32]. These generalized translations leave the magnetic structure invariant and lead to a generalized Bloch theorem. Therefore the Bloch spinors can still be characterized by a **k** vector in the Brillouin zone, and can be written as

$$\psi_k(\mathbf{r}) = e^{i\mathbf{kr}} \begin{pmatrix} e^{-i\mathbf{qr}/2} u_k(\mathbf{r}) \\ e^{+i\mathbf{qr}/2} d_k(\mathbf{r}) \end{pmatrix}. \quad (3)$$

The functions $u_k(\mathbf{r})$ and $d_k(\mathbf{r})$ are invariant with respect to lattice translations having the same role as for normal Bloch functions. Due to this generalized Bloch theorem the spin spirals can be studied within the chemical unit cell and no large super-cells are needed. Although the chemical unit cell can be used, the presence of the spin spiral lowers the symmetry of the system. Only the space-group operations that leave invariant the wave vector of the spiral remain. When considering the general spin space groups, i.e., taking the spin rotations into account, the space-group operations which reverse the spiral vector together with a spin rotation of $\pi$ around the $x$ axis are symmetry operations [32].

Although the original formulation of the local-spin-density approximation of the density-functional theory allowed noncollinear magnetic order, first-principles calculations for this aspect have begun only recently (for a review, see Ref. 33). One application has been the study of noncollinear ground states, for example, in γ-Fe (Refs. 34–36) or in frustrated antiferromagnets [37,38]. In

addition, the noncollinear formulation enables studies of finite-temperature properties of magnetic materials. Since the dominant magnetic excitations at low temperatures are spin waves which are noncollinear by nature, it is possible to determine the magnon spectra and ultimately the Curie temperature from first principles [39–43]. Recently, the noncollinear magnetic configurations were investigated in the Heusler alloys $Ni_2MnGa$, $Ni_2MnAl$ [31] and IrMnAl [44]. The total energies for different spin spirals were calculated and the ground-state magnetic structures were identified.

*Magnetocrystalline anisotropy*. Magnetic anisotropy is an important parameter, since in many instances their usefulness is determined by the magnetic anisotropy, i.e., by the extent to which the magnetization retains its orientation in response to magnetic field. As the most important magnetic anisotropy, the magnetocrystalline anisotropy is related to the crystal symmetry of a material. The magnetocrystalline anisotropy energy (MAE) describes the tendency of the magnetization to align along specific spatial directions rather than to randomly fluctuate over time. The MAE determines the stability of the magnetization in bulk as well as nanoparticle systems. Extensive studies of ferromagnetic bulk materials and thin films have highlighted the MAE dependence on crystal symmetry and atomic composition. Whereas the exchange interaction among electron spins is purely isotropic, the orbital magnetization, via the spin-orbit interaction, connects the spin magnetization to the atomic structure of a magnetic material, hence giving rise to magnetic anisotropy [45].

The calculation of the magnetocrystalline anisotropy energy has been a long-standing problem. A first theory of the MAE in Fe and Ni was formulated by Brooks [46] and Fletcher [47], who emphasized that an energy band picture, in which the effect of spin-orbit (SO) coupling is taken into account in a perturbative way, could provide a coupling of the magnetization orientation to the crystallographic axes of approximately the right order of magnitude. In this pioneering work the band structure was oversimplified to three empirical bands [46,47]. Recent investigations [48–52] elaborated the MAE problem using ab initio calculated energy bands obtained within the local-spin density approximation to the density functional theory. Although it is beyond doubt that LSDA energy bands are superior to empirical bands, it turned out that calculating the MAE from first principles poses a great computational challenge. The prime obstacle is the smallness of the MAE of only a few meV/atom, a value which ought to result as the difference of two total energies for different magnetization directions, which are both of the order of $4 \cdot 10^4$ eV/atom. Owing to this numerical problem, it remained at first unclear if the LSDA could at all describe the MAE correctly, since the wrong easy axis was obtained for *hcp* Co and *fcc* Ni [48]. Recent contributions aimed consequently at improving the numerical techniques [50,53], and the correct easy axis was obtained for *hcp* Co, but not for *fcc* Ni [50]. Halilov *et al.* [51] reported an *ab* initio investigation of the magnetocrystalline anisotropy energy in *bcc* Fe and *fcc* Co and Ni. They introduce the spin-orbit scaling technique, which yields the correct easy axis for Fe and Co, but a vanishing MAE for Ni.

The internal energy of ferromagnetic materials depends on the direction of spontaneous magnetization. We consider here one part of this energy, the MAE, which possesses the crystal symmetry of the material. For the material exhibiting uniaxial anisotropy, such as a hexagonal or tetragonal crystals, the MAE can be expressed as [48]

$$E(\theta) = K_1 \sin^2\theta + K_2 \sin^4\theta + K_3' \sin^6\theta + \\ + K_3 \sin^2\theta \cos[6(\varphi + \psi)] + \ldots \quad (4)$$

where $K_i$ is the anisotropy constant of the $i$th order, $\theta$ and $\varphi$ are the polar angles of the Cartesian coordinate system where the $c$ axis coincides with the $z$ axis (the Cartesian coordinate system was chosen such that the $x$ axis is rotated through 90° from the hexagonal axis) and $\psi$ is a phase angle.

Both the dipolar interaction and the spin-orbit coupling give rise to the MAE, the former contributing only to the first-order constant $K_1$. Hear, we deal with the MAE caused only by the spin-orbit interaction. Both magneto-optical effects and MAE have a common origin in the spin-orbit coupling and exchange splitting. Thus, a close connection between the two phenomena seems plausible.

The MAE is, in this paper, defined as the difference between two self-consistently calculated fully relativistic total energies for two different crystallographic directions, $E(\theta) - E_{<001>}$. To attain good convergence in the total energy a large number of **k** points has to be used in the calculations. In the present work the total energy has been calculated with an accuracy high enough to be able to resolve the difference in total energies for different spin directions.

*X-ray magnetic circular dichroism*. Using straightforward symmetry considerations it can be shown that all magneto-optical phenomena (XMCD, MO Kerr and Faraday effects) are caused by the symmetry reduction, in comparison to the paramagnetic state, caused by magnetic ordering [54]. This symmetry lowering has consequences only when spin-orbit coupling is considered in addition. Therefore, in order to calculate the XMCD properties one has to account for both magnetism and SO coupling at the same time when dealing with the electronic structure of the material considered.

Within the one-particle approximation, the absorption coefficient $\mu$ for incident x rays is determined by the probability of electron transitions from an initial core state (with wave function $\psi_j$ and energy $E_j$) to a final unoccupied states (with wave functions $\psi_{n\mathbf{k}}$ and energies $E_{n\mathbf{k}}$) as

$$\mu_j^{\lambda}(\omega) = \sum_{n\mathbf{k}} |\langle \Psi_{n\mathbf{k}} | \mathcal{J}_{\lambda} | \Psi_j \rangle|^2 \, \delta(E_{n\mathbf{k}} - E_j - \hbar\omega)\theta(E_{n\mathbf{k}} - E_F), \tag{5}$$

where $\hbar\omega$ is the photon energy, $\lambda$ its polarization and $\mathcal{J}_{\lambda} = -e\boldsymbol{\alpha}\mathbf{a}_{\lambda}$ being the dipole electron–photon interaction operator, where $\boldsymbol{\alpha}$ are Dirac matrices, $\mathbf{a}_{\lambda}$ is the $\lambda$ polarization unit vector of the photon vector potential $[a_{\pm} = 1/\sqrt{2}(1, \pm i, 0)$, $a_z = (0,0,1)]$. (Here $+/-$ denotes, respectively, left and right circular photon polarizations with respect to the magnetization direction in the solid).

Concurrent with the x-ray magnetic circular dichroism experimental developments, some important magneto-optical sum rules have been derived in recent years [55–58]. For the $L_{2,3}$ edges the $l_z$ sum rule can be written as [59]

$$\langle l_z \rangle = n_h \frac{4 \int\limits_{L_3+L_2} d\omega(\mu_+ - \mu_-)}{3 \int\limits_{L_3+L_2} d\omega(\mu_+ + \mu_-)} \tag{6}$$

where $n_h$ is the number of holes in the $d$ band $n_h = 10 - n_d$, $\langle l_z \rangle$ is the average of the magnetic quantum number of the orbital angular momentum. The integration is taken over the whole $2p$ absorption region. The $s_z$ sum rule is written as

$$\langle s_z \rangle + \frac{7}{2}\langle t_z \rangle = n_h \frac{\int\limits_{L_3} d\omega(\mu_+ - \mu_-) - 2\int\limits_{L_3} d\omega(\mu_+ - \mu_-)}{\int\limits_{L_3+L_2} d\omega(\mu_+ + \mu_-)} \tag{7}$$

where $t_z$ is the $z$ component of the magnetic dipole operator $\mathbf{t} = \mathbf{s} - 3\mathbf{r}(\mathbf{r}\cdot\mathbf{s})/|\mathbf{r}|^2$ which accounts for the asphericity of the spin moment. The integration $\int\limits_{L_3}(\int\limits_{L_2})$ is taken only over the $2p_{3/2}(2p_{1/2})$ absorption region.

*Crystal structure*. $Mn_3CuN$ at room temperature crystallizes in the cubic perovskite-type structure with $Pm\bar{3}m$ space group (No. 221). Mn atoms being at the face centers, Cu atoms at the corners, and N atoms at the body center (see Fig. 1). The Mn atoms have two N nearest neighbors at the 1.948 Å distance. The second coordination consists of 8 Mn atoms and 4 Cu atoms at the 2.755 Å.

The paramagnetic to ferromagnetic phase transition in $Mn_3CuN$ at $T_C$= 143 K is accompanied by a structural change from the cubic to the tetragonal lattice. The Mn moments in the low temperature ferromagnetic phase $P4/mmm$ space group, No. 123) constitute a noncollinear magnetic structure: $Mn_1$ canting from the $c$ axis to [111] direction, the $Mn_2$ and $Mn_3$ ferromagnetically align to the $c$ axis (Fig. 2). In the low temperature tetragonal structure Mn–N interatomic distances are slightly increased in comparison with the high temperature cubic phase up to the 1.954 Å. $Mn_1$ atoms are surrounded by two $Mn_2$ and two $Mn_3$ atoms at the 2.743 Å distance and four $Mn_1$ atoms at the 2.763 Å distance.

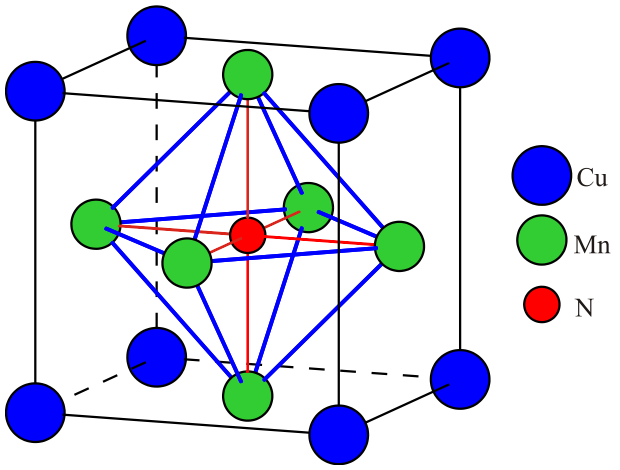


*Fig. 1*. (Color online) Cubic perovskite-type crystal structure of $Mn_3CuN$ at room temperature.

The details of the computational method are described in Refs. 59,60, and here we only mention several aspects. The calculations were performed for the experimentally observed lattice constants ($a$ = 3.896 Å for the cubic perovskite-type structure and $a$ =3.9075 Å $c/a$ =0.9853 for the low temperature tetragonal phase) using the spin-polarized linear-muffin-tin-orbital (LMTO) method [60,61] with the combined correction term taken into account. We used the von Barth–Hedin parametrization [62] for the exchange-correlation potential. Brillouin zone (BZ) integrations were performed using the improved tetrahedron method [63] and the charge self-consistency was obtained with 405 irreducible **k**-points. To improve the potential we include additional empty spheres both in the cubic

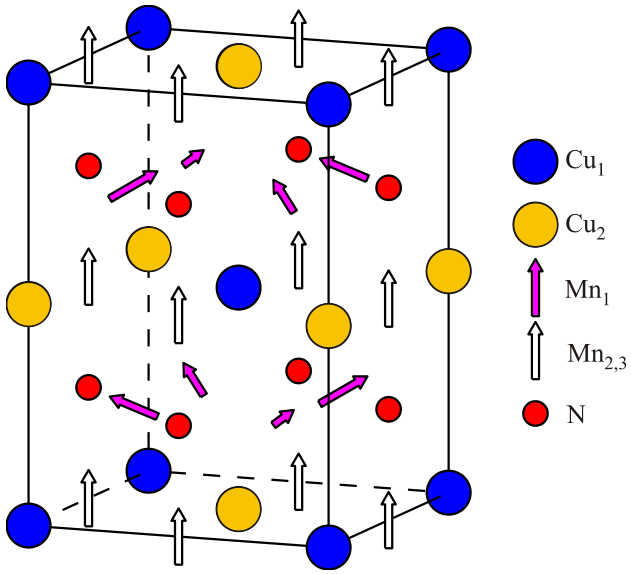


*Fig. 2*. (Color online) Low temperature magnetic structure of $Mn_3CuN$.

perovskite-type structure and the low temperature tetragonal phase. The basis consisted of Mn and Cu *s*, *p*, *d* and *f*; N *s*, *p*, *d* and empty spheres *s*, and *p* LMTO's.

The intrinsic broadening mechanisms have been accounted for by folding the XMCD spectra with a Lorentzian. For the finite lifetime of the core hole a constant width $\Gamma_c$, in general from Ref. 64, has been used. The finite apparative resolution of the spectrometer has been accounted for by a Gaussian of 0.6 eV.

## 3. Results and discussion

### *3.1. Energy band structure*

The total and partial density of states (DOS) of cubic hypothetical ferromagnetic $Mn_3CuN$ are presented in Fig. 3. The occupied part of the valence band can be subdivided into several regions. N 2*s* states appear between –17.6 and –15.9 eV. Cu 3*d* states are fully occupied and cross the N 2*p* bands in a very narrow energy interval from –4.6 to –1.5 eV. N 2*p* states extend from –8.6 eV up to 9 eV. The states in the energy range –4.5 to 5.5 eV are formed by Mn *d* states. The crystal field at the Mn site ($D_{4h}$ point symmetry) causes the splitting of *d* orbitals into three singlets $a_{1g}$ and $b_{1g}$ ($3z^2-1$ and $x^2-y^2$), $b_{2g}(xz)$ and a doublet $e_g(xy, yz)$. The $a_{1g}-b_{1g}$ and $b_{2g}-e_g$ splittings are negligible in comparison with its width in LSDA calculations. One should mention that there is quite a small N 2*p* – Mn *d* hybridization in the valence bands below the Fermi level.

$Mn_3CuN$ in the cubic perovskite type crystal structure has a local magnetic moments of 2.283 $\mu_B$ on Mn, 0.230 $\mu_B$ on Cu and –0.115 $\mu_B$ on N. The orbital moments are equal to 0.013 $\mu_B$, 0.003 $\mu_B$ and 0.0002 $\mu_B$ on the Mn, Cu and N sites, respectively. The interaction between the transition metals is ferromagnetic, leading to a total calculated moment of 6.963 $\mu_B$.

$Mn_3CuN$ partial DOS's for the low temperature tetragonal structure are presented in Fig. 4. For this crystal structure the spin magnetic moments are of 2.625 $\mu_B$ on the noncollinear $Mn_1$ atom sites, 2.390 $\mu_B$ on the collinear $Mn_{2,3}$ ones, 0.144 $\mu_B$ on Cu and –0.068 $\mu_B$ on N sites. The orbital moments are equal to –0.037 $\mu_B$, –0.003 $\mu_B$, –0.019 $\mu_B$ and 0.002 $\mu_B$ on the $Mn_1$, $Mn_{2,3}$, Cu and N sites, respectively.

Figure 5 presents the variation of Mn 3*d* spin (upper panel) and orbital (middle panel) magnetic moments at the $Mn_1$ and $Mn_{2,3}$ sites with the canting $Mn_1$ angle. The $Mn_1$ 3*d* orbital moments are negative for all the angle interval and reach its maximum absolute value at around 40°. The $Mn_{2,3}$ 3*d* orbital moments increase when the $Mn_1$ canting angle changes from 0° to 35°, and then decrease with further increasing of the canting angle, cross the zero at 60° and oscillate around zero up to 90°. The 3*d* spin moments are also show different angle behavior for the $Mn_1$ and $Mn_{2,3}$ sites (Fig. 5(a)). The $Mn_1$ 3*d* spin magnetic moments are larger for all the angle interval with the largest difference between the $Mn_1$ and $Mn_{2,3}$ spin moments when both the moments align along the *c* axis.

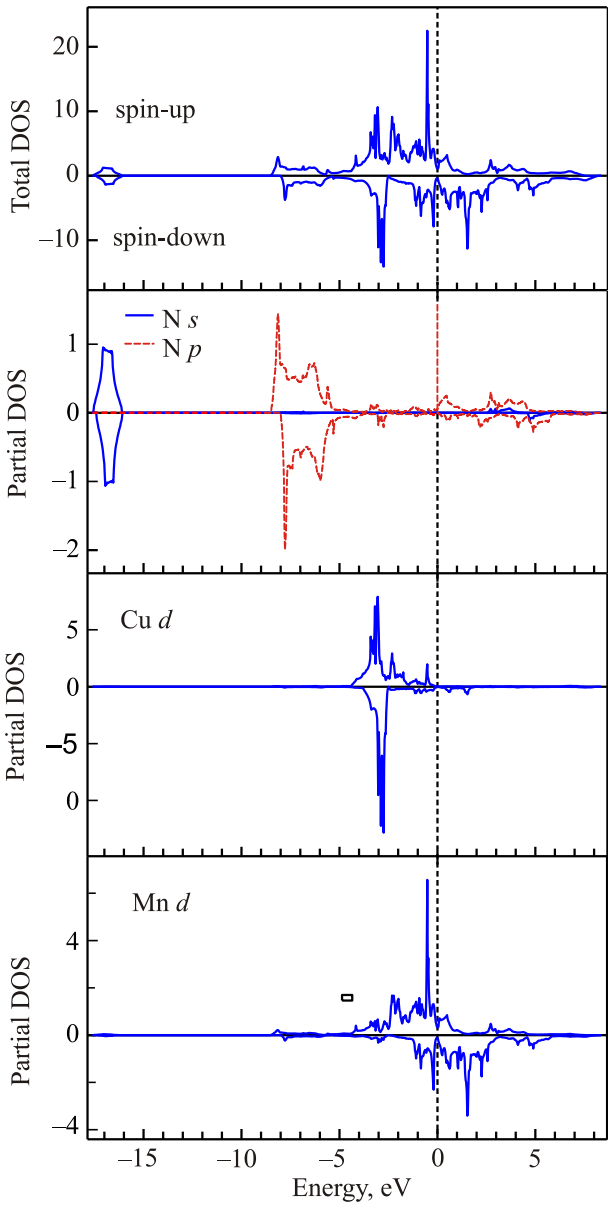


*Fig. 3.* (Color online)The total (in states/(cell eV)) and partial (in states/(atom eV)) ferromagnetic density of states of $Mn_3CuN$ in the cubic perovskite-type structure. The Fermi energy is at zero.

The lower panel (c) shows the magnetocrystalline anisotropy energy with the canting $Mn_1$ angle. We found that the ground state for the low-T phase of $Mn_3CuN$ is two Cu moments and two Mn ($Mn_2$ and $Mn_3$) moments ferromagnetically aligned to the *c* axis while four $Mn_1$ magnetic moments are canted by ±76.2° from the *c* axis to [111] direction (Fig. 2). It is important to note that this ground state with the canted $Mn_1$ magnetic moments is very stable. Quite a large energy of 5.5 meV/unit cell is needed to transit from the ground state with the canted $Mn_1$ magnetic moments to the state with all the magnetic

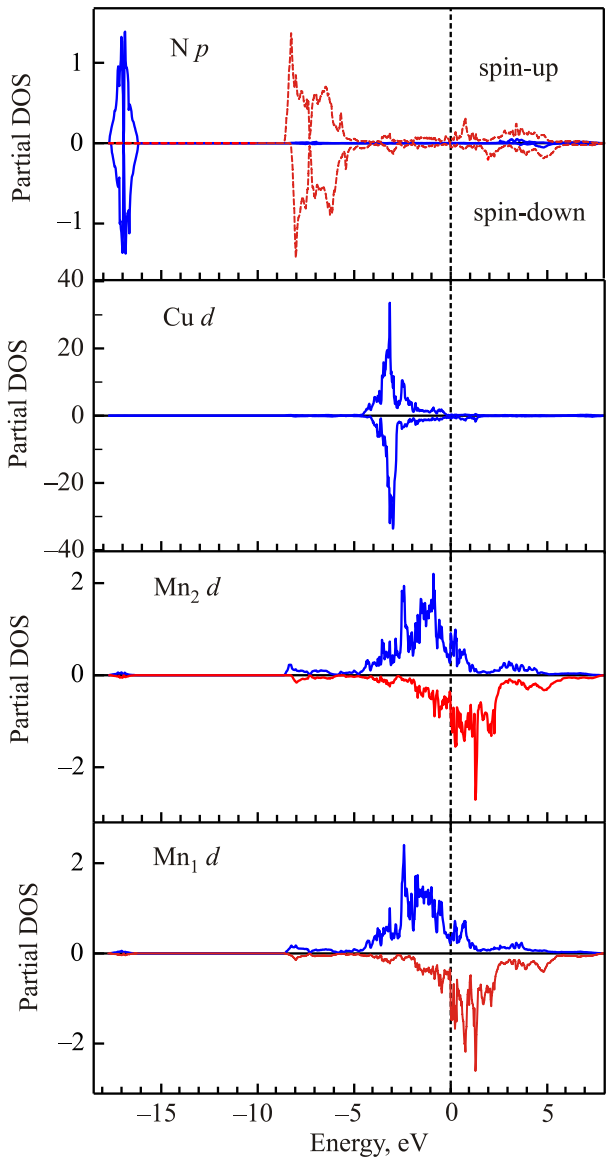


*Fig. 4*. (Color online) Partial density of states (in states/(atom eV)) of $Mn_3CuN$ in the low temperature non-collinear tetragonal structure. The Fermi energy is at zero.

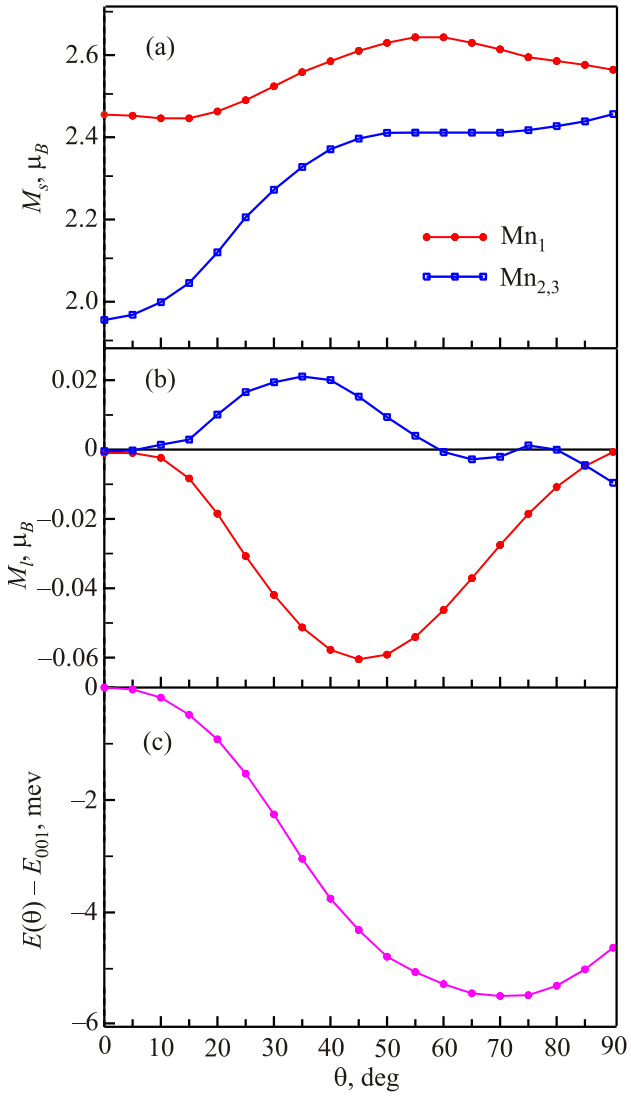


Fig. 5. (Color online) Variation of Mn 3*d* spin (a) and orbital (b) magnetic moments at the $Mn_1$ and $Mn_{2,3}$ sites with the canting $Mn_1$ angle. The lower panel shows the magnetocrystalline anisotropy energy with the canting $Mn_1$ angle.

moments oriented along the *c* axes. This fact helps to explain the magnetization experiments carried out by Takenaka *et al*. Ref. 29. They investigated the element-selective magnetization defined as peak-height difference between the positive $L_2$ peak and the negative $L_3$ peak. They found that the magnetic-field dependence for Cu is different from that for Mn. The $H$ dependence of the peak-height difference is characterized by a sharp increase at the low-field region for both Mn and Cu. However, the peak-height difference for Cu saturates at 2 kOe, whereas that for Mn shows only a kink at 2 kOe and continues to increase without saturation up to 19 kOe. Authors conclude that the two Cu and two ferromagnetically aligned $Mn_{2,3}$ moments are considered to saturate at a magnetic field of 2 kOe. However, the four counting $Mn_1$ magnetic moments $Mn_1$ considered to induce relatively weak magnetization under a magnetic field, resulting in the absence of saturation in the bulk magnetization up to 19 kOe. To reach the magnetic saturation, in other words to align all the magnetic moments along the *c* direction, one needs the energy much larger than provided by the magnetic field of 19 kOe.

On the other hand, the magnetocrystalline anisotropy energy which has been estimated by the difference of total energies between the states with spin orientation along and perpendicular to the *c* axes was found to be rather small in $Mn_3CuN$ reaching 0.5 meV/unit cell in agreement with the suggestion of Takenaka *et al*. Ref. 29.

### *3.2. XMCD spectra*

At the core level edge XMCD is not only element-specific but also orbital specific. For 3*d* transition metals, the electronic states can be probed by the *K*, $L_{2,3}$ and $M_{2,3}$

x-ray absorption and emission spectra. According to the dipole selection rules only the transitions with $\Delta l = \pm 1$, $\Delta j = 0, \pm 1$ are allowed [59]. Therefore only electronic states with an appropriate symmetry contribute to the absorption and emission spectra under consideration.

Figure 6 shows the theoretically calculated Mn $L_{2,3}$ x-ray absorption spectra (XAS) as well as XMCD spectra in $Mn_3CuN$ in comparison with the corresponding experimental data obtained by Takenaka *et al.* [29]. In order to compare the relative amplitudes of the $L_{2,3}$ XMCD spectra we first normalize the theoretically calculated x-ray absorption spectra to the experimental ones taking into account the background scattering intensity [65]. The LSDA describes reasonably well the shapes of the XAS spectra at the Mn $L_{2,3}$ edge (Fig. 6(a)). Because of the electric dipole selection rules the major contribution to the absorption at the $L_3$ edge stems from the transitions $2p_{3/2} \to 5d_{5/2}$, with a weaker contribution from $2p_{3/2} \to 5d_{3/2}$ transitions. For the latter case the corresponding $2p_{3/2} \to 5d_{3/2}$ radial matrix elements are only slightly smaller than for the $2p_{3/2} \to 5d_{5/2}$ transitions. The angular matrix elements, however, strongly suppress the $2p_{3/2} \to 5d_{3/2}$ contribution. Therefore the

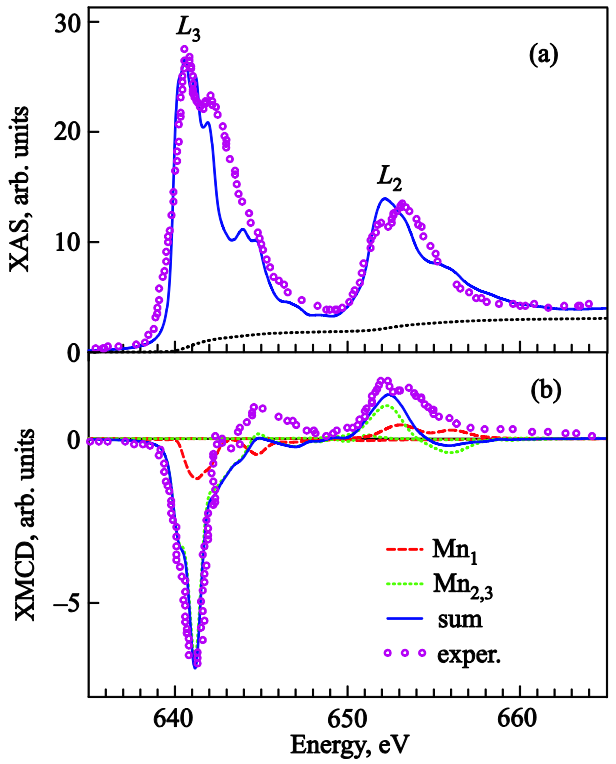


*Fig. 6.* (Color online) The theoretically calculated isotropic absorption spectra of $Mn_3CuN$ at the Mn $L_{2,3}$ edges for the low temperature tetragonal structure (full blue line) in comparison with the experimental spectrum [29] (circles) measured at 20 K in the external magnetic field $H$ = 19 kOe. The dotted line shows the theoretically calculated background spectrum (a); the experimental XMCD spectrum [29] measured at 20 K in the external magnetic field $H$ = 19 kOe (circles) and theoretically calculated XMCD spectra for the low temperature tetragonal structure (b).

contribution to the XMCD spectrum at the $L_3$ edge from the transitions with $\Delta j = 0$ is one order of magnitude smaller than the transitions with $\Delta j = 1$ [59]. The experimental x-ray absorption $L_3$ spectrum have three peaks around 640.5, 642 and 645 eV, which are well reproduced by the theoretical calculations. The intensity of the second fine structure at 642 eV is slightly underestimates by the theoretical calculations.

Figure 6 (b) shows the experimental XMCD spectrum [29] measured at 20 K and the theoretically calculated one using the LSDA approximation for the low-T tetragonal phase. The theory is in good agreement with the experimental measurements, although the calculated magnetic dichroism is somewhat too small at 645 eV in comparison with the experimental measurements. The XMCD spectra at the $L_{2,3}$-edges are mostly determined by the strength of the SO coupling of the initial $2p$-core states and spin-polarization of the final empty $3d_{3/2,5/2}$ states while the exchange splitting of the $2p$-core states as well as the SO coupling of the $3d$-valence states are of minor importance for the XMCD at the $L_{2,3}$ edge of $3d$ transition metals [59]. Although the number of $Mn_1$ atoms which are canted ±72.2° from the $c$ axis to [111] direction is two times larger than the number of ferromagnetically aligned $Mn_2$ and $Mn_3$ atoms (Fig. 2) the main contribution to the $L_{2,3}$ XMCD spectra comes from the $Mn_{2,3}$ atoms (Fig. 6(b)).

Takenaka *et al.* [29] apply sum rules [Eqs. (6),(7)] to estimate the spin and orbital moments at the Mn and Cu sites. They found extremely small spin magnetic moment at the Mn site $m_s^{Mn} = 0.27\mu_B$ which is almost one order of magnitude smaller than obtained in our band structure calculations. The Mn $L_3$ and the $L_2$ spectra in $Mn_3CuN$ are strongly overlapped therefore the decomposition of a corresponding experimental $L_{2,3}$ spectrum into its $L_3$ and $L_2$ parts is quite difficult and can lead to a significant error in the estimation of the magnetic moments using the sum rules. Besides, the experimentally measured Mn $L_{2,3}$ x-ray absorption spectra have background scattering intensity and the integration of the corresponding XASs may lead to an additional error in the estimation of the magnetic moments using the sum rules. Besides, XMCD sum rules are derived within an ionic model using a number of approximations [59,66]. It is interesting to compare the spin moments obtained from the theoretically calculated XAS and XMCD spectra through sum rule [Eq. (7)] with directly calculated LSDA values in order to avoid additional experimental problems. We obtain $m_s^{Mn_1} = 1.84\ \mu_B$, $m_s^{Mn_{2,3}} = 1.17\ \mu_B$ from sum rules. These values are significantly smaller than the corresponding magnetic moments derived from the band structure calculations (2.63 $\mu_B$ and 2.39 $\mu_B$ for $Mn_1$ and $Mn_{2,3}$, respectively). However, they are still much larger than the experimental value $m_s^{Mn} = 0.27\ \mu_B$ [29]. One of the possible reasons of such small experimental magnetic moment might be a disorder effect. This question still needs an additional experimental investigation.

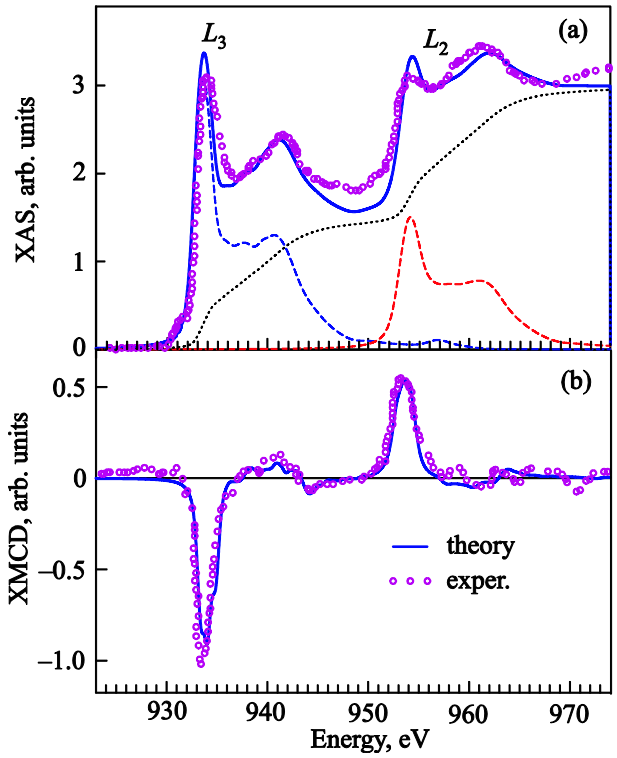


*Fig. 7*. (Color online) The theoretically calculated isotropic absorption spectra of $Mn_3CuN$ at the Cu $L_3$ (blue dashed line) and Cu $L_2$ (red dashed line) edges for low temperature tetragonal structure in comparison with the experimental spectrum [29] (circles) measured at 20 K in the external magnetic field $H$ = 19 kOe. The full blue line presents the theoretically calculated Cu $L_{2,3}$ XAS with taking into account the background spectrum (dotted black line) (a); the experimental XMCD spectrum at Cu $L_{2,3}$ edges [29] measured at 20 K in the external magnetic field $H$ = 19 kOe (circles) and the theoretically calculated XMCD spectra for the low temperature tetragonal structure (b).

Figure 7 shows the theoretically calculated Cu $L_{2,3}$ edge x-ray absorption spectra as well as XMCD spectra in $Mn_3CuN$ in comparison with the corresponding experimental data [29]. The experimentally measured Cu $L_{2,3}$ XAS spectra possess rather large background intensity (Fig. 7(a)). Both the $L_3$ and $L_2$ XAS spectra contain intensive narrow low energy peaks and wide high energy shoulders which reflect the energy distribution of Cu 3*d* empty states (see Fig. 4). Figure 7(b) shows the theoretically calculated XMCD spectra at the Cu $L_{2,3}$ edges in comparison with the experimentally measured ones [29]. The theory shows a very good agreement with the experiment for the x-ray absorption as well as for the XMCD.

## 4. Summary

In $Mn_3CuN$ a magnetic phase transition occurs at $T_C$ =143 K, which has been classified as a first-order transition from a paramagnetic phase to a ferromagnetic one with a noncollinear magnetic structure. The transition is accompanied by a structural change from the cubic to the tetragonal lattice.

We have studied the electronic structure in the high-T ferromagnetic cubic phase and low temperature non-collinear phase of $Mn_3CuN$ perovskite compound in the LSDA approximation by means of an *ab initio* fully-relativistic spin-polarized Dirac linear muffin-tin orbital method. The magnetic unit cell of low-T ferromagnetic $Mn_3CuN$ contains two magnetic moments due to Cu and six magnetic moments due to Mn; two Cu moments and two Mn moments ($Mn_2$ and $Mn_3$) are ferromagnetically aligned along the $c$ axis while other four $Mn_1$ magnetic moments are canted from the $c$ axis to [111] direction. We found that the ground state corresponds to the canting angle $\Theta = \pm 76.2°$. We investigated the influence of the $Mn_1$ canting angle on the total energy and 3*d* spin and orbital magnetic moments at Mn sites. We found that the $Mn_1$ 3*d* orbital moments are negative for all the angle interval and reach its maximum absolute value at around 40°. The $Mn_{2,3}$ 3*d* orbital moments increase when the $Mn_1$ canting angle changes from 0° to 35°, and then decrease with further increasing of the canting angle, cross the zero value at 60° and oscillate around zero up to 90°. The 3*d* spin moments also show different angle behavior for the $Mn_1$ and $Mn_{2,3}$ sites. The $Mn_1$ 3*d* spin magnetic moments are larger for all the angle interval with the largest difference between the $Mn_1$ and $Mn_{2,3}$ spin moments when both the moments align along the $c$ axis.

We have studied theoretically the x-ray absorption and x-ray magnetic circular dichroism spectra at the Mn and Cu $L_{2,3}$ edges in the low temperature noncollinear phase of $Mn_3CuN$. The calculated spectra show excellent agreement with the experiment. We show that although the number of $Mn_1$ atoms which are canted by the ±76.2° from the $c$ axis to [111] direction is two times larger than the number of ferromagnetically aligned $Mn_2$ and $Mn_3$ atoms the main contribution to the $L_{2,3}$ XMCD spectra comes from the $Mn_{2,3}$ atoms.

## Acknowledgments

This work was supported by the National Academy of Sciences of Ukraine in the framework of the State Target Scientific and Technology Programs "Nanotechnology and Nanomaterials" for 2010-2014 (No. 0277092303) and Implementation and Application of Grid Technologies for 2009-2013 (No. 0274092303).

1. M. Guillot, R.P. Pauthenet, and C.R. Acad, *Sci. (Paris)* **258**, 3242 (1964).
2. J.P. Bouchaud, R. Fruchart, and C.R. Acad, *Sci. (Paris)* **261**, 458 (1965).
3. J.J. Pierre, J.P. Bouchaud, R. Fruchart, M. Guillot, H. Bartholin, F. Chaisse, and C.R. Acad, *Sci*. (*Paris*) **261**, 655 (1965).

4. J.P. Bouchaud, R. Fruchart, P. Pauthenet, M. Guillot, H. Bartholin, and F. Chaisse, *J. Appl. Phys*. **37**, 971 (1966).
5. D. Fruchart, E.F. Bertaut, F. Sayetat, M.N. Eddine, R. Fruchart, and J.P. Senateur, *Solid State Commun*. **8**, 91 (1970).
6. A. Kenmotsu, T. Shinohara, and H. Watanabe, *J. Phys. Soc. Jpn*. **32**, 377 (1972).
7. D. Fruchart, E.F. Bertaut, B.L. Clerc, L.D. Khoi, P. Veittet, G. Lorthioir, M.E. Fruchart, and R. Fruchart, *J. Solid State Chem*. **8**, 182 (1973).
8. D. Fruchart and B.F. Bertaut, *J. Phys. Soc. Jpn*. **44**, 781 (1978).
9. T. Kaneko, T. Kanomata , and K. Shirakawa, *J. Phys. Soc. Jpn*. **56**, 4047 (1987).
10. R.C. O'Handley, S.J. Murray, M. Marioni, H. Nembach, and S.M. Allen, *J. Appl. Phys*. **87**, 4712 (2000).
11. R. Kainuma, Y. Imano, W. Ito, Y. Sutou, H. Morito, S. Okamoto, O. Kitakami, K. Oikawa, A. Fujita, T. Kanomata, and K. Ishida, *Nature* **439**, 957 (2006).
12. E.F. Wasserman, in: *Ferromagnetic Materials*, K.H.J. Buschow and E.P. Wohlfarth (eds.), Elsevier, Amsterdam (1990), Vol. 5, p. 237.
13. O. Tegus, E. Brück, K.H.J. Buschow, and F.R. de Boer, *Nature* **415**, 150 (2002).
14. A. Fujita, S. Fujieda, Y. Hasegawa, and K. Fukamichi, *Phys. Rev. B* **67**, 104416 (2003).
15. A.E. Clark, in: *Ferromagnetic Materials*, E.P. Wohlfarth (ed.), Elsevier, Amsterdam, (1980), Vol. 1, p. 531.
16. K. Takenaka and H. Takagi, *Appl. Phys. Lett*. **87**, 261902 (2005).
17. K. Takenaka and H. Takagi, *Mater. Trans*. **47**, 471 (2006).
18. R.J. Huang, L.F. Li, F.S. Cai, X.D. Xu, and L.H. Qian, *Appl. Phys. Lett*. **93**, 081902 (2008).
19. K. Takenaka, K. Asano, M. Misawa, and H. Takagi, *Appl. Phys. Lett*. **92**, 011927 (2008).
20. Y. Sun, C. Wang, Y.C. Wen , L.H. Chu, H. Pan, M. Nie, and M.B. Tang, *J. Am. Ceram. Soc*. **93**, 2178 (2010).
21. T. Shibayama and K. Takenaka, *J. Appl. Phys*. **109**, 07A928 (2011).
22. M. Barberon, R. Madar, E. Fruchart, G. Lorthioir, and R. Fruchart, *Mater. Res. Bull*. **5**, 1 (1970).
23. K. Asano, K. Koyama, and K. Takenaka, *Appl. Phys. Lett*. **92**, 161909 (2008).
24. J.P. Jardin and J. Labbé, *J. Phys. (Paris)* **36**, 1317 (1975).
25. K. Motizuki and H. Nagai, *J. Phys. C* **21**, 5251 (1988).
26. M. Shirai, Y. Ohata, N. Suzuki, and K. Motizuki, *Jpn. J. Appl. Phys., Suppl. 32-3* **32**, 250 (1993).
27. M. Takahashi and J. Igarashi, *Phys. Rev. B* **67**, 245104 (2003).
28. L. Hua, L. Wang, and L.F. Chen, *J. Phys.: Condens. Matter* **22**, 206003 (2010).
29. K. Takenaka, T. Shibayama, A. Ozawa, T. Hamada, T. Nakamura, K. Kodama, and T. Kinoshita, *J. Appl. Phys*. **110**, 023909 (2011).
30. V.N. Antonov, B.N. Harmon, A.N. Yaresko, and A.P. Shpak, *Phys. Rev. B* **75**, 165114 (2007).
31. J. Enkovaara, A. Ayuela, J. Jalkanen, L. Nordstrom, and R.M. Nieminen, *Phys. Rev. B* **67**, 054417 (2003).
32. L.M. Sandratskii, *J. Phys.: Condens. Matter* **3**, 8565 (1991).
33. L. Sandratskii, *Adv. Phys*. **47**, 91 (1999).
34. L. Sandratskii and J. Kübler, *J. Phys.: Condens. Matter* **4**, 6927 (1992).
35. D.M. Bylander and L. Kleinman, *Phys. Rev. B* **59**, 6278 (1999).
36. K. Knöpfle, L. Sandratskii, and J. Kübler, *Phys. Rev. B* **62**, 5564 (2000).
37. P. Kurz, G. Bihlmayer, K. Hirai, and S. Blügel, *Phys. Rev. Lett*. **86**, 1106 (2001).
38. D. Hobbs and J. Hafner, *J. Phys.: Condens. Matter* **12**, 7025 (2000).
39. V.P. Antropov, M.I. Katsnelson, M. van Schilfgaarde, and B.N. Harmon, *Phys. Rev. Lett*. **75**, 729 (1995).
40. N.M. Rosengaard and B. Johansson, *Phys. Rev. B* **55**, 975 (1997).
41. M. Uhl and J. Kübler, *Phys. Rev. Lett*. **77**, 334 (1996).
42. S.V. Halilov, H. Eschrig, A.Y. Perlov, and P.M. Oppeneer, *Phys. Rev. B* **58**, 293 (1998).
43. M. Pajda, J. Kudrnovsky, I. Turek, V. Drchal, and P. Bruno, *Phys. Rev. B* **64**, 174402 (2001).
44. V.N. Antonov, B.N. Harmon, A.N. Yaresko, L.V. Bekenov, and A.P. Shpak, *Phys. Rev. B* **73**, 094445 (2006).
45. C. Hirjibehedin, C. Lin, A. Otte, M. Ternes, C. Lutz, and B. Jones, *Science* **317**, 1199 (2007).
46. H. Brooks, *Phys. Rev*. **58**, 909 (1940).
47. G.C. Fletcher, *Proc. R. Soc. London, Ser. A* **67**, 505 (1954).
48. G.H.O. Daalderop, P.J. Kelly, and M.F.H. Schuurmans, *Phys. Rev. B* **41**, 11919 (1990).
49. P. Strange, J.B. Staunton, B.L. Györffy, and H. Ebert, *Physica B* **172**, 51 (1991).
50. J. Trygg, B. Johansson, O. Eriksson, and J.M. Wills, *Phys. Rev. Lett*. **75**, 2871 (1995).
51. S.V. Halilov, A.Y. Perlov, P.M. Oppeneer, A.N. Yaresko, and V.N. Antonov, *Phys. Rev. B* **57**, 9557 (1998).
52. P. Ravindran, A. Delin, P. James, B. Johansson, J.M. Wills, R. Ahuja, and O. Eriksson, *Phys. Rev. B* **59**, 15680 (1999).
53. D.-S. Wang, R. Wu, and A.J. Freeman, *Phys. Rev. Lett*. **70**, 869 (1993).
54. W.H. Kleiner, *Phys. Rev*. **142**, 318 ().
55. G. van der Laan and B.T. Thole, *Phys. Rev. B* **38**, 3158 (1988).
56. B.T. Thole, P. Carra, F. Sette, and G. van der Laan, *Phys. Rev. Lett*. **68**, 1943 (1992).

57. P. Carra, B.T. Thole, M. Altarelli, and X. Wang, *Phys. Rev. Lett.* **70**, 694 (1993).
58. G. van der Laan and B.T. Thole, *Phys. Rev. B* **53**, 14458 (1996).
59. V. Antonov, B. Harmon, and A. Yaresko, *Electronic Structure and Magneto-Optical Properties of Solids*, Kluwer, Dordrecht (2004).
60. V.V. Nemoshkalenko and V.N. Antonov, *Computational Methods in Solid State Physics*, Gordon and Breach, Amsterdam (1998).
61. O.K. Andersen, *Phys. Rev. B* **12**, 3060 (1975).
62. U. von Barth and L. Hedin, *J. Phys. C* **5**,1629 (1972).
63. P.E. Blöchl, O. Jepsen, and O.K. Andersen, *Phys. Rev. B* **49**, 16223 (1994).
64. J.C. Fuggle and J.E. Inglesfield, *Unoccupied Electronic States. Topics in Applied Phys*., Springer, New York (1992), Vol. 69.
65. F.K. Richtmyer, S.W. Barnes, and E. Ramberg, *Phys. Rev*. **46**, 843 (1934).
66. V.N. Antonov, O. Jepsen, A.N. Yaresko, and A.P. Shpak, *J. Appl. Phys*. **100**, 043711 (2006).